pubs.acs.org/Biomac

Article

Self-Assembled Nanosized Vehicles from Amino Acid-Based Amphiphilic Polymers with Pendent Carboxyl Groups for Efficient Drug Delivery

Wenli Feng, Zixuan Huang, Xiaoxu Kang, Dongdong Zhao, Haofei Li, Guofeng Li,* Jiangtao Xu,* and Xing Wang*

Cite This: https://doi.org/10.1021/acs.biomac.1c01164

Read Online

ACCESS | Metrics & More | Article Recommendations | Supporting Information

ABSTRACT: Developing safe and efficient delivery vehicles for chemotherapeutic drugs has been a long-standing demanding. Amino acid-based polymers are promising candidates to address this challenge due to their excellent biocompatibility and biodegradation. Herein, a series of well-defined amphiphilic block copolymers were prepared by PET-RAFT polymerization of *N*-acryloyl amino acid monomers. By altering monomer types and the block ratio of the copolymers, the copolymers self-assembled into nanostructures with various morphologies, including spheres, rod-like, fibers, and lamellae via hydrophobic and hydrogen bonding interactions. Significantly, the nanoparticles (NPs) assembled from amphiphilic block copolymers poly(*N*-acryloyl-valine)-*b*-poly(*N*-acryloyl-aspartic acid) (PV-*b*-PD) displayed an appealing cargo loading efficiency (21.8−32.6%) for a broad range of drugs (paclitaxel, doxorubicin (DOX), cisplatin, etc.) due to strong interactions. The DOX-loaded PV-*b*-PD NPs exhibited rapid cellular uptake (within 1 min) and a great therapeutic performance. These drug delivery systems provide new insights for regulating the controlled morphologies and improving the efficiency of drug delivery.

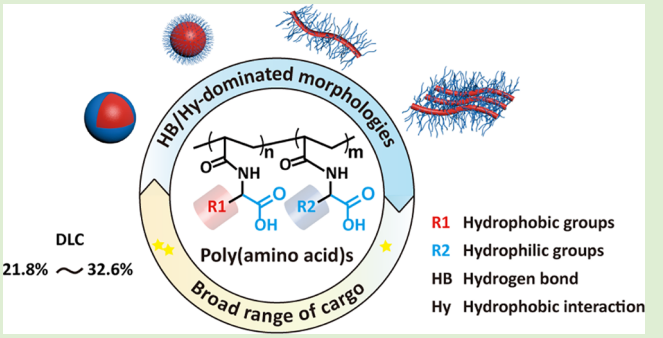

1. INTRODUCTION

Drug delivery systems (DDS) are highly desired in the development of nanomedicine.[1,2] A plethora of different loading strategies have been exploited in recent decades, such as network cross-linking,[3] mesoporous inorganic nanoparticles,[4] drug-polymer conjugates,[5] drug−drug conjugate nanomedicines,[6] and sequential nanoprecipitation technology.[7] However, despite enormous research efforts by scientists from various disciplines and substantial investments from industries,[8,9] only a limited number of nanomedicines have been approved by the U.S. Food and Drug Administration (FDA) for clinical uses.[10] The major obstacles to hinder the clinical translation of nanomedicines are drug loading (usually below 10 wt%), controlled release, safety, and so on.[11,12] Besides, there are still few common strategies for loading different drugs. Thus, a universal nanoparticle carrier system with high drug loading and controllable drug release abilities will be a demanding platform for circumventing many of the issues that plague nanotherapeutics.[13,14]

Amino acids, as the building block units of proteins, are valuable and versatile units for constructing drug delivery materials.[15,16] Since 1990s, Endo and Mori have been dedicated to developing amino acid-based polymers for diverse applications.[17−19] Amino acid moieties have been incorporated into polymer chains at two different locations, in the polymer main chains (polypeptides) through ring-opening polymerization of α-amino acid *N*-carboxyanhydride (NCA),[20−23] and on the side chains by converting amino acids into polymerizable vinyl monomers and subsequently polymerizing them using reversible deactivation radical polymerization,[24,25] or other viable methods.[26]

As of now, remarkable progress has been made in synthetic amino acids-based main chain polymers (polypeptides) that hold promises for drug, or gene delivery,[27−29] owing to its inherent biocompatibility and biomimetic features.[30,31] Deming et al.[32] have investigated the self-assembly behavior of poly(L-lysine)-*b*-poly(L-leucine) polypeptides. Priyadarsi et al.[33−35] designed and synthesized leucine-based copolymers for the production of various nanoobjects through self-assembly. These pioneering works have demonstrated the capability of amino acid-based amphiphilic block copolymers (BCPs) in the preparation of nanosized particles.[36] In contrast,

Received: September 6, 2021
Revised: September 24, 2021

Scheme 1. Schematic Illustration of the Synthetic Route of Homopolymers and Diblock Copolymer by PET-RAFT Polymerization and Their Assembled Morphologies and Cargo Loading Ability Depending on the Strong HB Interaction in Hydrophilic Fraction

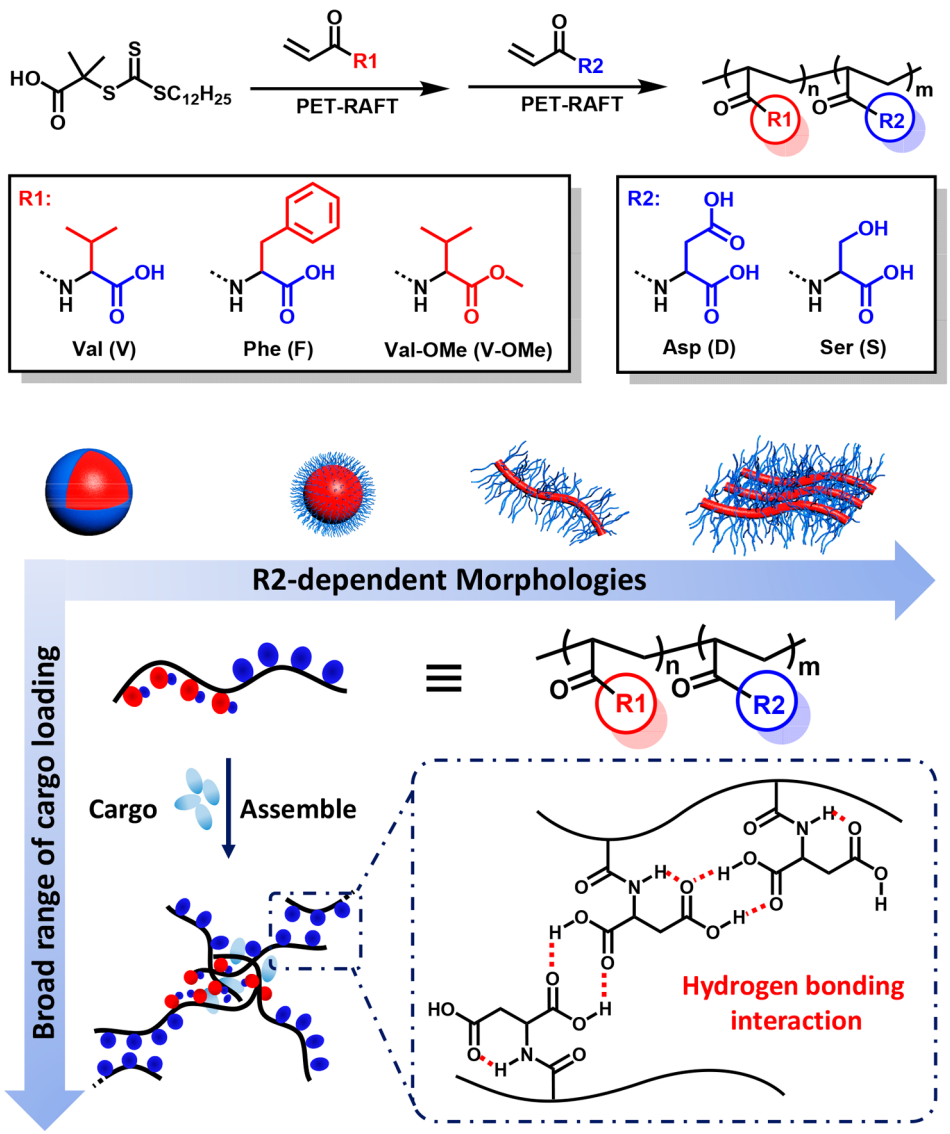

the self-assembly behavior of BCPs with amino acid substituents in the side chains are underexplored, which possess high-density pendent functional groups, providing a plethora of chelating or binding sites for diverse chemotherapeutic drugs through a variety of noncovalent interactions, such as aromatic stacking, hydrogen bonding, electrostatic and hydrophobic interactions.[37,38]

In our previous report,[39] we have established a robust photoinduced electron/energy transfer-reversible addition−fragmentation chain transfer (PET-RAFT) polymerization to precisely control the block sequences and low polydispersity without protecting the acid functionalities of *N*-acryloyl-amino acid monomers. Herein, we use this synthetic technique to prepare a series of poly(*N*-acryloyl amino acid) (PAA) polymers with desired block sequences/lengths and side functionalities and subsequently study their self-assembly behavior in aqueous solutions (Scheme 1). A range of morphologies of PAA nanoparticles (NPs) including spheres, rod-like, fiber, and lamellae have been obtained by changing the varieties of amino acid-based monomers and hydrophilic/hydrophobic block ratios. Interestingly, the assembled NPs from amphiphilic poly(*N*-acryloyl-valine)-*b*-poly(*N*-acryloyl-aspartic acid) (PV-*b*-PD) exhibit a high loading capacity for many types of cargos in that the strong intermolecular hydrogen bonding (HB) and hydrophilic/hydrophobic interactions. Moreover, in vitro cytotoxicity studies against mouse fibroblast cell line (L929) and the human hepatoma carcinoma cell line (HepG2) revealed these PAA NPs had excellent biocompatibility. Most significantly, the doxorubicin (DOX)-loaded PV-*b*-PD NPs (DOX@NPs) showed very fast endocytosis (within 1 min) and excellent killing performance toward cancer cells.

2. EXPERIMENTAL SECTION

Materials. All amino acids (≥97%), common solvents, and the mentioned cargos in the manuscript were purchased from Sigma-Aldrich (U.S.A.) and J&K Scientific. L929, HepG2 cells were purchased from Cell Resource Center, IBMS, CAMS/PUMC, Beijing,

https://doi.org/10.1021/acs.biomac.1c01164
Biomacromolecules XXXX, XXX, XXX−XXX

China. Cell culture media and detection reagents were purchased from Gibco BRL (Gaithersburg, MD, U.S.A.) and Dojindo (Japan).

Characterizations. $^{1}H/^{13}C$ NMR spectra were recorded on a 400 NMR spectrometer (Bruker AVANCE^{III}, Switzerland). The number (M_n) and weight (M_w) average molecular weight and molecular mass distribution ($Đ$) were determined using a Gel Permeation Chromatography (GPC, Waters, U.S.A.). UV−visible (UV−vis) spectra was carried out on a UV−vis spectrometer (U-4100, Hitachi, Japan). The hydrodynamic diameter (D_h) and polydispersity index (PDI) of the nanostructures dissolved in water was determined on a dynamic light scattering (DLS) instrument (ZetaSizer NanoZS90, Malvern, U.K.). Transmission electron microscopy (TEM, HT-7700, Hitachi, Japan) and scanning electron microscopy (SEM, JSM-7800F, JEOL, Japan) were used to observe the morphologies of nanostructures. The surface elements of the samples were determined by energy-dispersive spectroscopy (EDS, S-4700, Hitachi, Japan).

Synthesis of Amphiphilic Polymers. Concisely, all monomers, *N*-acryloyl-valine (V), *N*-acryloyl-aspartic acid (D), *N*-acryloyl-phenylalanine (F), *N*-acryloyl-serine (S), and *N*-acryloyl-valine methyl ester (V-OMe) were synthesized according to the procedure reported by our group.[39,40] Then the synthetic route of amphiphilic block copolymer was performed through PET-RAFT technique according our previous study (Scheme 1).[39] In a typical procedure (e.g., polymerization of PV) of PET-RAFT polymerization technique, V (1.0 g, 5.84 mmol), 2-(dodecylthiocarbonothioylthio)-2-methylpropionic acid (DDMAT; 42.5 mg, 0.11 mmol), tris[2-(pyridin-2-yl)phenyl]iridium ($Ir(ppy)_3$; 0.019 mg, 2.92×10^{-5} mmol), and 4 mL of dimethyl sulfoxide (DMSO) were added to a glass vial. After degassing for 20 min under a N_2 atmosphere, the reaction mixture was placed under blue light at room temperature for 4 h and then was quenched and purified in a dialysis bag (MWCO 1000 Da) against ethanol (EtOH). For the block copolymer (e.g., polymerization of PV-*b*-PD), the polymerization procedure was the same as that of PV synthesis, but PV was used as the macro-RAFT agent to instead of DDMAT. The length of the PD segment was tunable by varying the monomer feed ratio. All protocols were shown in Table S1. Last, the polymer was dried under vacuum to get a yellow solid. Yield: 85%. For GPC analysis, the methylated sample was prepared for the GPC measurements.[39]

Preparation of Nanostructures and Cargo-Loaded NPs. Polymer assemblies were prepared by nanoprecipitation from DMSO into deionized water and then dialyzed (MWCO 3500 Da dialysis bag) for 48 h to remove organic solvent. For the construction of cargo-loaded NPs, first, doxorubicin hydrochloride (DOX·HCl) has been neutralized by trimethylamine (TEA) to get hydrophobic DOX. Then, these cargos, coumarin 6 (C6), curcumin (CUR), paclitaxel (PTX), and DOX were dissolved in DMSO, and PV-*b*-PD was added to this series of solution and further self-assemble as outlined above. These concentrated aggregates were further diluted for DLS, SEM, and TEM studies and then frozen, lyophilized, and stored at 4 °C. The cargos loading quantification by UV−vis at 458 nm (C6), 425 nm (CUR), 227 nm (PTX), and 480 nm (DOX). Differently, cisplatin (CDDP)-loaded NPs were prepared according to the typical method.[11] Simply, CDDP was reacted with silver nitrate ($AgNO_3$) to get CDDP solution, which was then added dropwise into PV-*b*-PD aqueous solution under ultrasonic oscillation. The mixed solution was stirred for 72 h and then dialyzed (MWCO 3500 Da dialysis bag) for 48 h to remove unbounded CDDP. The loading quantification of CDDP was detected by a color reaction between CDDP and *o*-phenylenediamine (OPDA). The drug loading content (DLC, wt %) and drug loading efficiency (DLE, wt %) were calculated following the formula below:

$$\mathrm{DLC(wt\%)} = (\text{wt of loaded cargo}/\text{total wt of polymer and loaded cargo}) \times 100\%$$

$$\mathrm{DLE(wt\%)} = (\text{wt of loaded cargo}/\text{wt of cargo in feed}) \times 100\%$$

In Vitro Drug Release Studies. The drug release of the DOX@NPs was investigated using a typical dialysis method. A total of 5.0 mg of DOX@NPs dissolved in 5.0 mL of PBS was put into a dialysis bag (MW 3500 Da) and dialyzed in 20 mL of PBS with different pH (5.4, 6.0, 7.4) under slow stirring at 180 rpm. A total of 1.0 mL of the solution was taken away from the system and replaced with 1.0 mL of fresh PBS solution after a predetermined time. The absorbance intensity of the samples was recorded by UV−vis, and the amount of DOX released was calculated accordingly.

In Vitro Cytotoxicity Test. Cytotoxicity of the blank NPs and DOX@NPs against L929 cells and HepG2 cells was assayed by Cell Counting Kit-8 (CCK8). Typically, 5×10^4/mL of cells were seeded in a sterile 96-well plate and incubated at 37 °C for 24 h. Then, different concentrations of blank NPs and DOX@NPs in culture medium were added and further incubated for 24 and 48 h. Next, a CCK-8 test kit was coincubated for another 1 h. The absorbance of each solution was measured at 450 nm using Spectramax M5 spectrophotometer (Molecular Devices, Sunnyvale, CA). The cell viability was calculated according to the absorbance.

Cellular Uptake. Confocal laser scanning microscopy (CLSM) was used to investigate the cellular uptake and intracellular release behaviors of DOX@NPs. The HepG2 cells were seeded in a culture dish and allowed to adhere for 24 h. The medium was then replaced with free DOX·HCl or DOX@NPs solutions with a drug concentration of 2 $\mu g\ mL^{-1}$, and then cells were monitored at different time points. After being incubated for 4 h, the cells were washed with PBS and stained with the 2′-(*p*-ethoxypenenyl)-5-(4-methyl-1-piperazinyl)-5′-bibenzimidazole (Hoechst 33342) after fixing by 4% paraformaldehyde. Fluorescence images of cells were observed using CLSM.

Flow Cytometry Study. HepG2 cells were coincubated with free DOX·HCl or DOX@NPs (2 $\mu g\ mL^{-1}$) for 1 and 4 h. The cells were collected and resuspended in 1 mL of PBS. Endocytosis of free DOX·HCl or DOX@NPs was quantified by the flow cytometer (BD FACSAriaSORP).

3. RESULTS AND DISCUSSION

Synthesis of Amphiphilic Block Copolymers. The synthetic route of PAA copolymers is illustrated in Scheme 1. Amino acid-based acrylate monomers, V, D, F, V-OMe, and S, were first successfully prepared following the protocols in our previous report.[40,41] $^{1}H/^{13}C$ NMR and high-resolution

Table 1. Characterization Data for All Polymers Used in This Study

sample[a]	hydrophilic fraction[b] (%)	conversion[c] (%)	M_n[c] (kDa)	M_n[d] (kDa)	$Đ$[e]
PV_{31}	0	90	6.5	6.1	1.31
PV_{31}-*b*-PD_{13}	30	80	8.7	9.1	1.25
PV_{31}-*b*-PD_{24}	45	82	11.1	11.4	1.28
PV_{31}-*b*-PD_{35}	53	85	12.8	13.7	1.31
PV_{31}-*b*-PD_{55}	64	86	17.7	18.1	1.39
PV_{31}-*b*-PD_{68}	68	86	21.0	20.9	1.45
PF_{26}	0	91	6.3	6.6	1.41
PF_{26}-*b*-PD_5	16	85	7.9	7.6	1.31
PF_{26}-*b*-PD_{18}	41	94	9.8	10.5	1.35
PF_{26}-*b*-PD_{59}	69	86	17.6	19.4	1.62
PV-OMe_{40}	0	86	8.3	7.7	1.29
PV-OMe_{40}-*b*-PD_{30}	31	85	16.2	13.2	1.51
PV-OMe_{40}-*b*-PD_{157}	80	80	38.2	42.1	1.56
PV-OMe_{40}-*b*-PS_{34}	45	83	14.9	13.6	1.42
PV-OMe_{40}-*b*-PS_{157}	80	89	36.6	34.9	1.62

[a]The numbers in the subscript indicate the degrees of polymerization calculated by GPC. [b]Molar percentages of hydrophilic fraction in the amphiphilic diblock copolymers. [c]Determined by ^{1}H NMR spectroscopy. [d]Measured by GPC that is calibrated by polystyrene standards. [e]Molecular mass distribution ($Đ$) determined by GPC.

https://doi.org/10.1021/acs.biomac.1c01164
Biomacromolecules XXXX, XXX, XXX−XXX

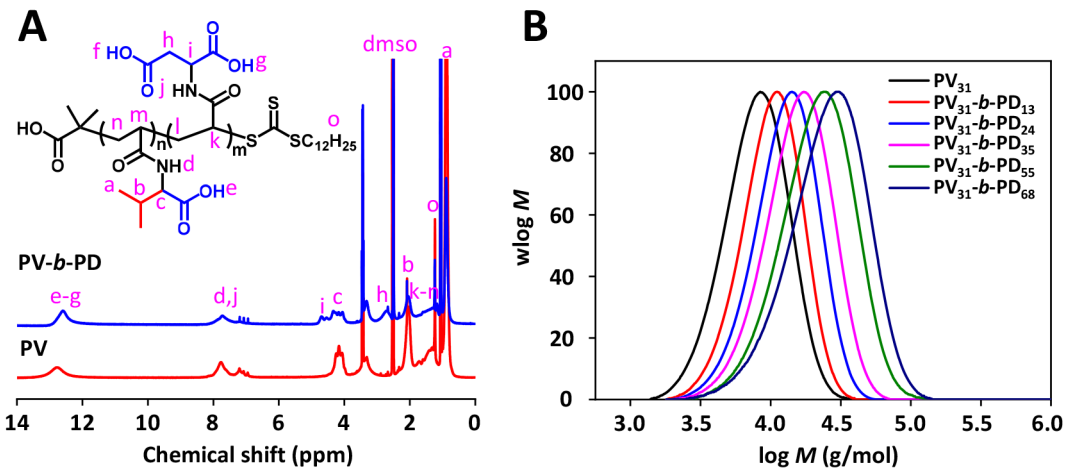

Figure 1. (A) ^{1}H NMR spectrum of PV_{31} macro-CTA (red line) and PV_{31}-*b*-PD_{24} copolymers (blue line; 400 MHz, DMSO-d_6 as solvent). (B) Molecular weight distributions of PV homopolymer and PV_{31}-*b*-PD_m copolymers (m = 0, 13, 24, 35, 55, 68) at different polymerization ratios. GPC analysis (THF used as eluent) was used to determine the molecular weight and dispersity of the polymers. Polystyrene standards were used for calibration.

mass spectroscopy were employed to confirm the chemical structure of all monomers. (Figures S1−S3). The copolymers were precisely synthesized via PET-RAFT polymerization technique. Taking PV-*b*-PD as an example, PV_{31} (M_n = 6.5 kg mol^{-1}, $Đ$ = 1.31, Table 1) macromolecular chain transfer agent (macro-CTA) was synthesized in DMSO via PET-RAFT polymerization using DDMAT as a CTA and $Ir(ppy)_3$ as the initiator.[39] Its degree of polymerization (DP) was determined by ^{1}H NMR and GPC. As shown in Figure 1A, by comparing the integrals of characteristic methylene protons "o" in the hydrocarbon tail of DDMAT and methyl protons "a" in valine monomer repeating units, the DP of PV was calculated to be 31, which was consistent with that calculated from the GPC-determined molecular weight (Table 1). Then, copolymer PV_{31}-*b*-PD_m (the subscript m denotes the DP of the D monomer) was synthesized with different fractions of PD (30−70 mol %) and characterized by ^{1}H NMR (Figure 1A) and GPC (Figure 1B). The GPC traces of these resulting copolymers exhibited a shift from low molecular weight (macro-CTA PV_{31}) to high molecular weight, confirming the successfully synthesis of diblock copolymers. We further characterized the composition of these polymers through EDS (Figure S4). Increasing the proportion of the hydrophilic block PD, the atomic percentage of the entire polymer has the same trend relative to the theoretical value, which further proves the successful polymerization of PV-*b*-PD. Additionally, the other three diblock copolymers, poly(*N*-acryloyl-phenylalanine)-*b*-poly(*N*-acryloyl-aspartic acid) (PF-*b*-PD), poly(*N*-acryloyl-valine methyl ester)-*b*-poly(*N*-acryloyl-aspartic acid) (PV-OMe-*b*-PD), and poly(*N*-acryloyl-valine methyl ester)-*b*-poly(*N*-acryloyl-serine) (PV-Ome-*b*-PS), were also synthesized using the same protocols. All copolymers were characterized by ^{1}H NMR and GPC (Table 1 and Figures S5 and S6), showing high conversions (78−95%) and a narrow molecular mass distribution ($Đ$, 1.25−1.65).

Self-Assembly Behavior of PV-*b*-PD. The self-assembly behavior of PV-*b*-PD was first investigated. The self-assembly was carried out in a mixed solvent system, DMSO/water. The solution gradually turned turbid and ultimately milky-white. SEM and TEM analysis showed that the macro-CTA PV_{31} homopolymer formed a spherical nanostructure with an average diameter of 350 nm (Figure 2A). DLS (Figure S7) showed similar results that the D_h of the spherical nanostructure was approximately 400 nm with a narrow distribution (0.19, Table S2). Interestingly, various morphologies of assembled nanostructures including sphere, rod-like, fiber, lamellae were obtained while increasing the fractions of second block PD (Figure 2B−F). When the PD fraction was 30%, the copolymers (PV_{31}-*b*-PD_{13}) exhibited a spherical nanostructure with an average diameter of 280 nm (Figure 2B), which is smaller than that of PV_{31} nanostructure. These nanostructures had rough edges and connected to each other to form a necklace-like aggregates (Figure 2B). As the PD fraction increased further to 45% (PV_{31}-*b*-PD_{24}), the sizes of the necklace-like spherical nanostructure decreased to approximately 180 nm (Figure 2C); but at the same time, most of the spheres interconnected with each other and transformed to rods with ∼320 nm widths and ∼1.3 μm lengths. While increasing PD fractions (53%, PV_{31}-*b*-PD_{35}), the extended polymer chains may intertwine with each other to form nanofibers with an average D_h of ∼30 nm and a length exceeding several micrometers (Figure 2D). When PD fraction was more than 60% (64% for PV_{31}-*b*-PD_{55}, 68% for PV_{31}-*b*-PD_{68}), copolymers gradually transitioned to microscale lamellar structure (Figure 2E,F).

PAA has multiple functional groups, such as carboxyl, amino, and alkyl groups, which will govern its self-assembly through hydrophilic/hydrophobic and HB interactions.[24,42,43] A plausible explanation for the PV-*b*-PD assembling process was illustrated in Scheme 2. Initially, when dialyzing against water, hydrophobic moieties (alkyl groups and isopropyl groups) in PV_{31} were driven to aggregate and form hydrophobic domains by a force balance involving the repulsive interactions of the corona chains, the interfacial energy between the core and the solvent, and the deformation of the core-forming blocks in the core (Scheme 2a).[44,45] The copolymers possess lots of carboxyl groups and amide groups, which could form stable hexacycle-like HB interactions against water.[46,47] These interactions affect the hydrophilic repulsion of the shell segments and dominate the assembling behavior of PV-*b*-PD (Scheme 2b−d). The spherical nanostructure, therefore, was compressed into a smaller size, accompanied

https://doi.org/10.1021/acs.biomac.1c01164
Biomacromolecules XXXX, XXX, XXX−XXX

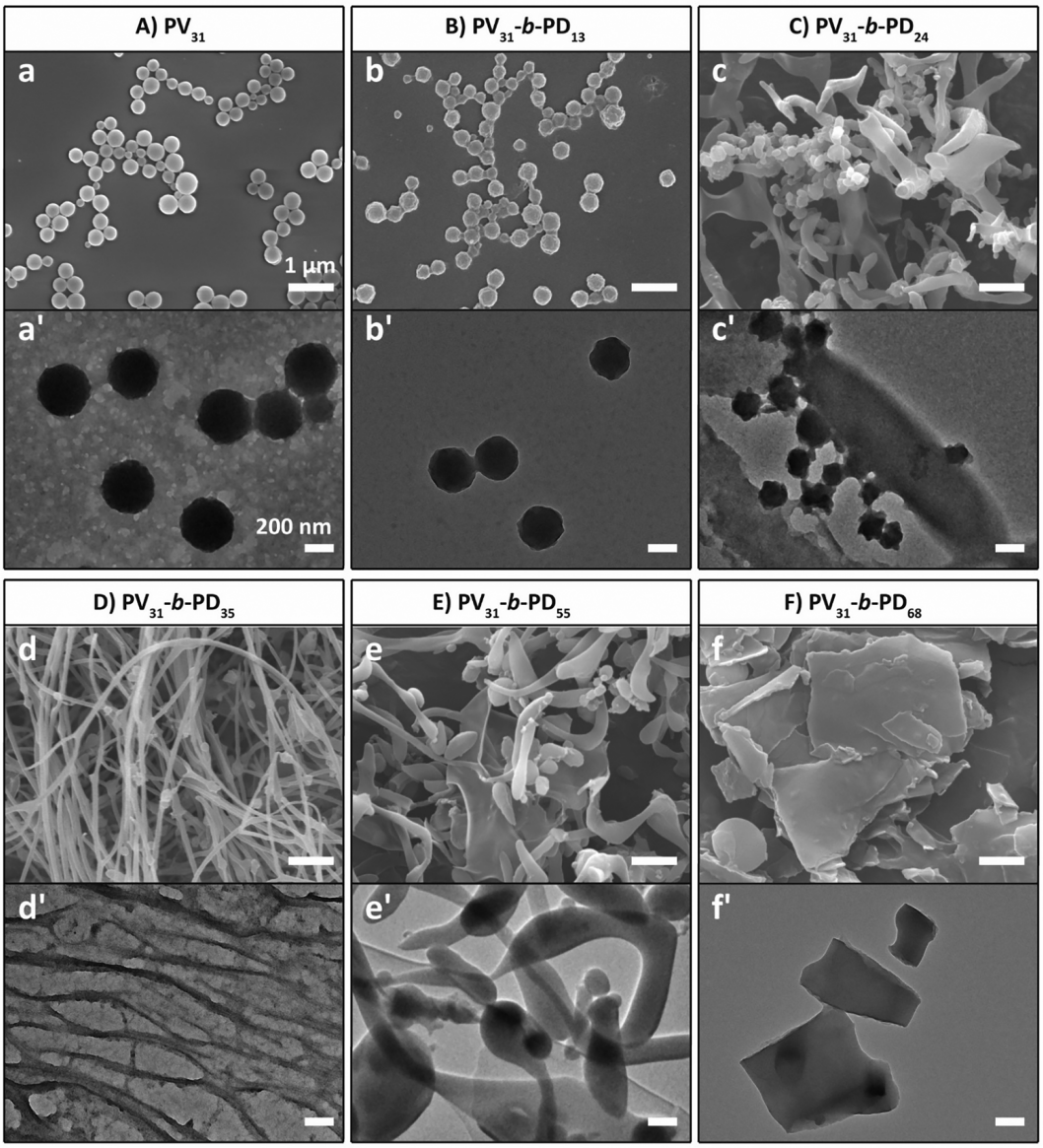

Figure 2. Morphologies of self-assembled nanostructures of PV_{31}-*b*-PD_m in an aqueous solution. SEM images (a–f, scale bars = 1 μm) and TEM images (a′–f′, scale bars = 200 nm) corresponding to the copolymers with m = 0 (A), 13 (B), 24 (C), 35 (D), 55 (E), and 68 (F), respectively.

by the strengthened HB interaction and hydrophilic repulsion, while increasing PD fractions. Moreover, this behavior also might be related to the change of the micelles' curvatures. According to the packing parameter theory of flexible amphiphilic copolymer assembly,[48] the core-forming PV was a short volume fraction, which drove the copolymers to form aggregates in a low interfacial energy situation. Increasing PD block lengths of the PV-*b*-PD copolymer induced higher repulsion, which favors a decrease in the radius of curvature and contributed to the formation of smaller nanostructures (Scheme 2a,b). Simultaneously, the spherical nanostructure is forced to connect together, gradually transfering to rods, fibers, and lamella because of a strong HB interaction and the minimization of interfacial energy (Scheme 2c,d). The aggregates tend to form lower surface energy morphology. With the increase of the hydrophilic PD polymer chain, the assembled morphology of the copolymer PV-*b*-PD changes from a spherical structure to a rod-like structure. The rod-like structure is conducive to increasing the specific surface area, thereby reducing the free energy of the interface, so that the energy of the system was reduced and became stable.[49] The balance of these two different forces leads to the formation of various morphologies. As PD increases, the corona volume fraction increases, resulting in the reduction of curved interfaces. The polymer chains, therefore, have to adopt new arrangements to reduce their stretching, leading to a morphological transition from spheres to fibers and further lamellae.

Effects of Hydrophobic Interaction on the Self-Assembly of PAAs. To further elucidate the nanostructure formation, a hydrophobic monomer F was selected to synthesize the hydrophobic block, as the first block (PF_{26}-*b*-PD_m) attributed that the phenyl group in F is more hydrophobic than isopropyl in V. The self-assembled nanostructure presented a sphere morphology for homopolymer PF_{26} and underwent a change from sphere to fiber for diblock copolymers, which may be related to the introduction of aromatics leading to a strengthened hydrophobic interaction

https://doi.org/10.1021/acs.biomac.1c01164
Biomacromolecules XXXX, XXX, XXX–XXX

Scheme 2. Morphological Transitions of Self-Assembled Amphiphilic PV_{31}-*b*-PD_m Copolymers[a]

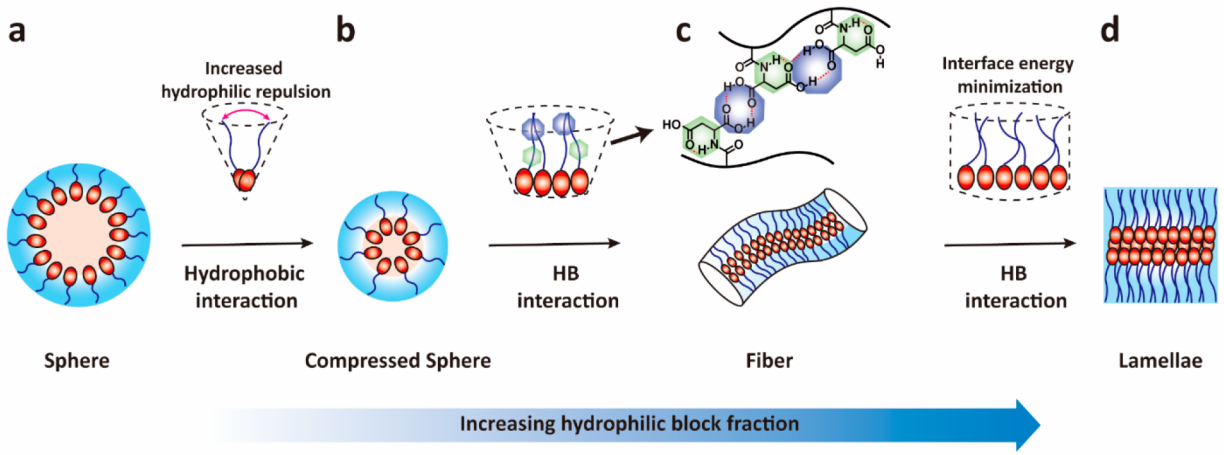

[a](a, b) Assembly of PV-*b*-PD molecules into spheres. (c) Transformation of the aggregation into a rod. (d) Transformation of the rod-like into lamellae. Schematic diagram not to scale.

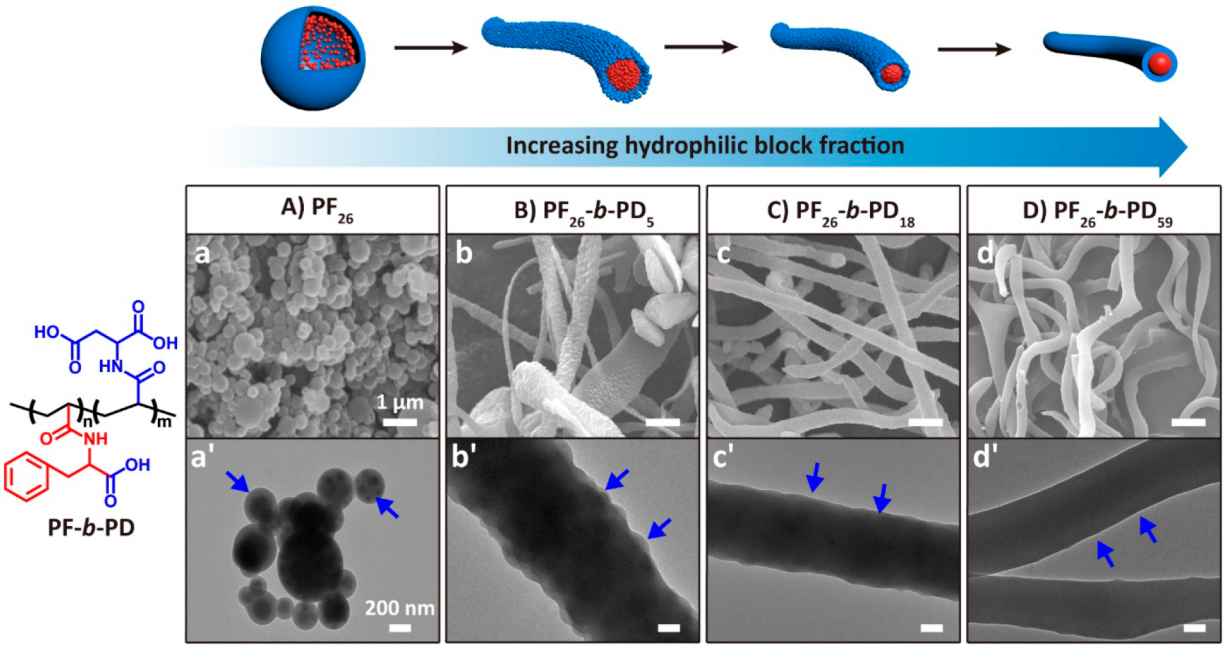

Figure 3. Morphology studies of assembled nanostructures of PF_{26}-*b*-PD_m. SEM images (a–d, scale bars = 1 μm) and TEM images (a′–d′, scale bars = 200 nm) corresponding to PF_{26}-*b*-PD_m, with m = 0 (A), 5 (B), 18 (C), and 59 (D), respectively. The blue arrows exhibited the roughness of the surface of nanostructures.

and $\pi-\pi$ stacking.[50−52] As shown in Figure 3A, the PF_{26} homopolymer self-assembled into spheres with a ∼110 nm diameter. Several high-density cores were observed in the nanostructure interiors, which might stem from the stable $\pi-\pi$ stacking. Increasing the PD length (16%, PF_{26}-*b*-PD_5), the spherical nanostructure was connected to each other and spliced into an irregular fiber (Figure 3B), suggesting that the stacking parameters of copolymer PF_{26}-*b*-PD_5 increased with the introduction of PD.[48] DLS measurements exhibited a similar result (Figure S7). In other words, the interfacial attraction between hydrophobic blocks rather than the hydrophilic repulsion between hydrophilic blocks was dominant in PF_{26}-*b*-PD_5 assemble system. Therefore, the boundary area of each copolymer in the microstructure decreased, resulting in an increased stacking parameter.[53] Additionally, we reasoned that fiber elongation happens through the nanostructure fusion process because the integral spherical nanostructure could be clearly discovered on the surface of the fibers.[54] The fiber morphology might be mediated through a secondary assembly process. First, PF_{26}-*b*-PD_5 assembled as a spherical nanostructure because of the strong hydrophobic interaction. Second, the "pearl necklace" nanostructure formed over the adhesive collisions of the spherical nanostructure by HB interaction and then evolved to a worm-like nanostructure because of the interfacial tension.[55] Further increasing the PD fraction to 41% (PF_{26}-*b*-PD_{18}), the assembled fibers became more uniform and thinner (Figure 3C). The outline of the micelles could hardly be observed on the surface of the fibers. When the PD fraction was increased to 69% (PF_{26}-*b*-PD_{59}), the enhanced HB interaction

https://doi.org/10.1021/acs.biomac.1c01164
Biomacromolecules XXXX, XXX, XXX−XXX

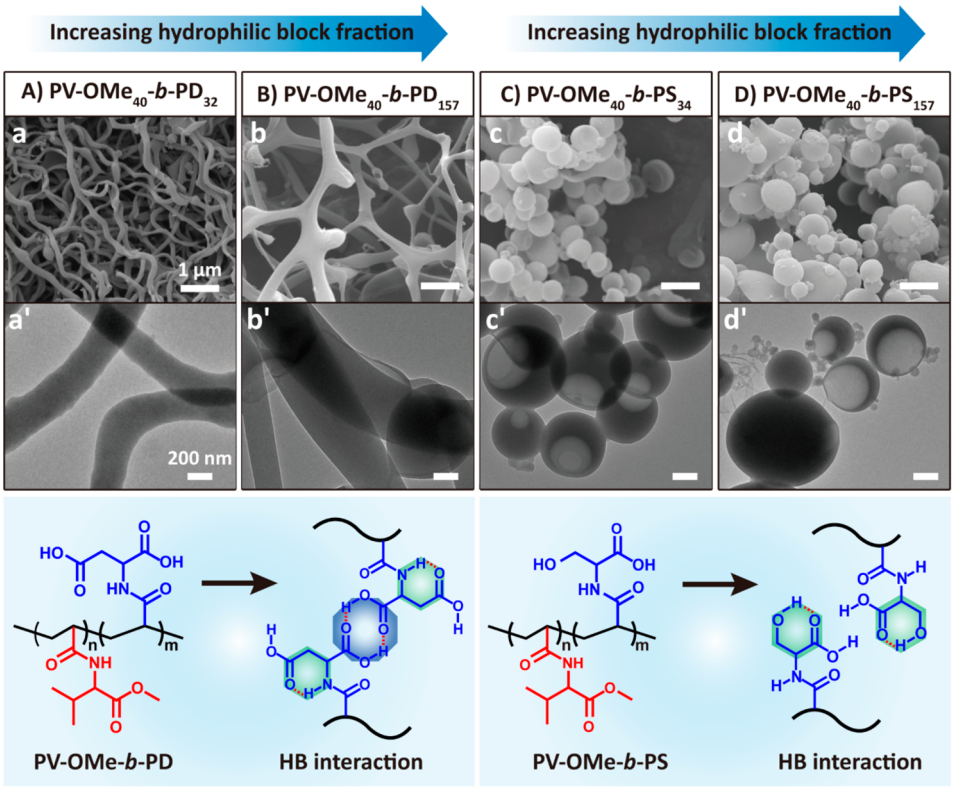

Figure 4. Morphology studies of assembled nanostructures of PV-OMe-*b*-PX$_m$ (X = D/S). SEM images (a–d, scale bars = 1 μm) and TEM images (a′–d′, scale bars = 200 nm) corresponding to PV-OMe$_{40}$-*b*-PD$_m$, with m = 32 (A) and 157 (B), and PV-OMe$_{40}$-*b*-PS$_m$, with m = 34 (C) and 157 (D), respectively.

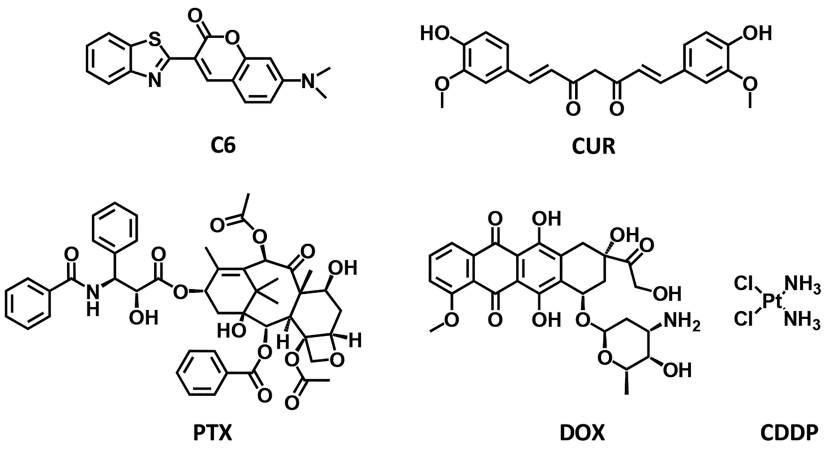

Figure 5. Chemical structures of investigated cargo loaded into NPs: C6, CUR, PTX, DOX, and CDDP.

Table 2. Characterization of DLC and DLE for All Cargo-Loaded NPs Used in This Study

cargo	size (d, nm)	PDI	DLC (%)	DLE (%)
C6	153.2	0.104	21.8	70.0
CUR	154.2	0.115	24.2	80.0
PTX	143.5	0.095	26.4	72.0
DOX	255.2	0.178	32.6	97.6
CDDP	198.1	0.158	31.2	78.2

dominated the assemble behaviors and might directly force the formation of fibers (Figure 3D). Thus, the surface of fibers becomes relatively smooth (blue arrows in Figure 3). Though involvement of these interactions was not established completely, the assemble behaviors of PF-*b*-PD indicated that increased hydrophobic interaction and $\pi-\pi$ stacking could strengthen the interfacial attraction between hydrophobic blocks that maintained the spherical appearance. But, the interaction was difficult to overcome nanostructure aggregation induced by HB bonding.[56] The addition of carboxyl groups drives copolymers to assemble into fibers because of the interfacial tension.

Effects of the HB Interaction on the Self-Assembly of PAAs. Carboxylic acid hydrogen bonding between the neighboring nanostructures could drive the nanostructures to form higher order morphologies.[55] Therefore, the effect of

https://doi.org/10.1021/acs.biomac.1c01164
Biomacromolecules XXXX, XXX, XXX–XXX

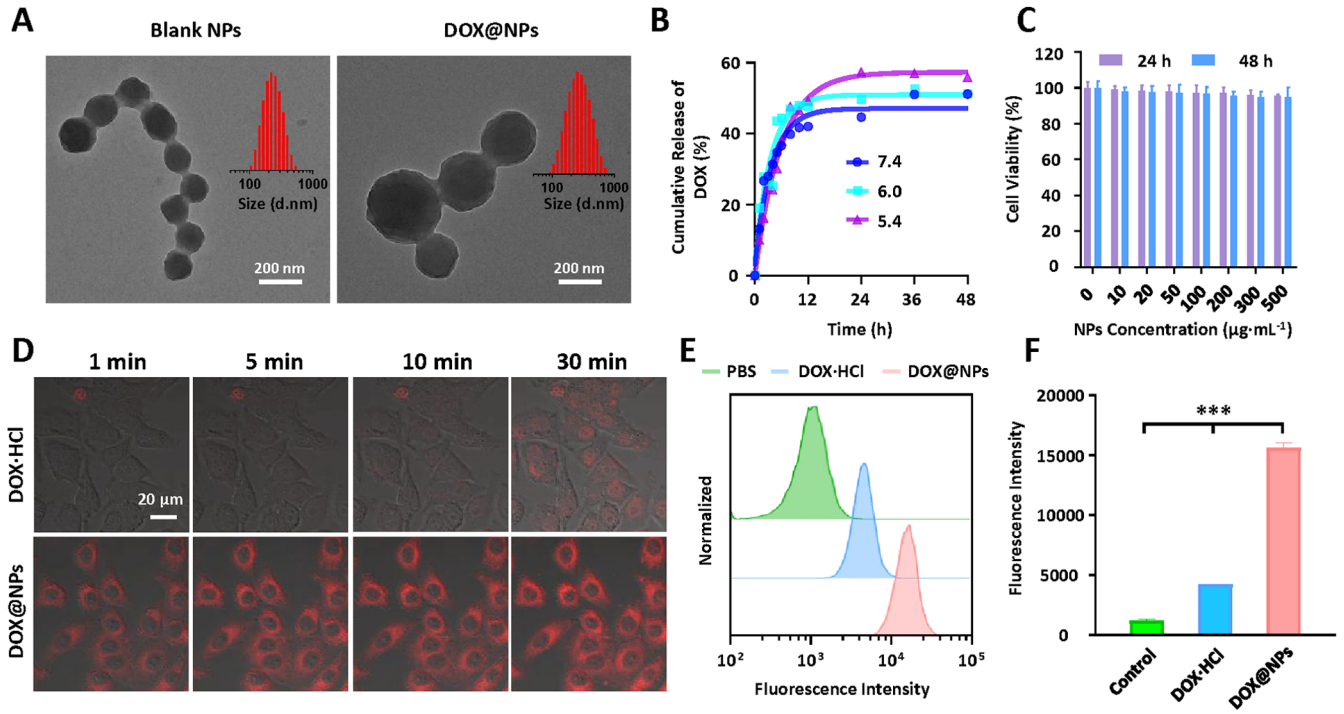

Figure 6. Characterization of DOX@NPs based on copolymer PV_{31}-*b*-PD_{13}. (A) TEM and DLS characterization of blank NPs and DOX@NPs. Scale bars = 200 nm. (B) In vitro cumulative drug release profiles of DOX@NPs under different pH values (mean ± SD, n = 3). (C) The cytotoxicity of blank NPs against HepG2 cells. (D) CLSM was utilized to real-time monitoring the cellular uptake behaviors of HepG2 cells treated with free DOX·HCl and DOX@NPs. The DOX concentration was 2 μg mL^{-1}, scale bar = 20 μm. (E) Flow cytometry and (F) statistics of cellular uptake of DOX after treating with free DOX·HCl and DOX@NPs for 1 h. Data were expressed as mean ± SD from three independent experiments. The p value was determined by two-way ANOVA analysis: ***$p < 0.001$.

carboxylic acid groups on the assembling behaviors was further investigated. V-OMe with the carboxylic acid being converted into an ester was used as the hydrophobic monomer instead of the monomer F. The synthetic PV-OMe was a hydrophobic polymer and could not form a stable nanostructure by itself (Figure S8). Interestingly, the copolymer PV-OMe-*b*-PD formed uniform nanoscale fibers rather than spheres, regardless of the PD fraction (44% or 80%, Figures 4A,B and S8). These results may be attributed to the interfacial attraction of hydrophobic blocks being dominant in the PV-OMe-*b*-PD assemble system; carboxyl groups in PD segments reinforce the intermolecular connection by the enhanced HB interaction, which is in favor of fiber formation. Accordingly, PS was chosen as the hydrophilic segment, in which the content of the carboxyl group in the hydrophilic segment could be reduced. As shown in Figure 4C, the obtained copolymers (PV-OMe_{40}-*b*-PS_{34}, PS fraction was 45%) were assembled into a vesicle nanostructure with a ∼500 nm diameter. Increasing the proportion of PS to 80% (PV-OMe_{40}-*b*-PS_{157}), the sphere became larger but still maintained the vesicular morphology (Figure 4D). These results indicated that the stacking parameter of PV-OMe-*b*-PS (1/2∼1) was higher than that of PV-OMe-*b*-PD (1/3∼1/2), which was mainly caused by the decrease the hydrophilic repulsion of PS segment.[57,58] The PD possessing dual-carboxyl groups and amide group in one unit could easily form complex intra/intermolecular HB interactions.[55] In contrast, PS possesses a hydroxyl group, which was a strong HB donor that could first form a stable six-membered ring intramolecular HB with the carboxyl group (Figure 4).[59] Attenuated intermolecular HB interaction, therefore, reduced interference for the assembly behavior of PV-OMe-*b*-PS copolymers. These results provided convincing evidence that the HB interaction of carboxyl groups rather than the hydrophilic/hydrophobic interaction dominates the assembly behavior of PAA copolymers. Increasing the amount of carboxyl groups drove the copolymers to form a nanoscale fiber and even lamellar structures. When the DP of the hydrophobic segment is set as ∼30, while that of the hydrophilic segment is set as ∼15 (the fraction was ∼50%), it was easy to get a PAA copolymer with a sphere nanostructure.

Cargo Loading. The existence of side carboxyl groups is significant for improving the drug-loading capacity.[60] Then, we examined the potentiality of PV_{31}-*b*-PD_{13} assembled NPs as vehicles for cargo delivery. Five representative cargos were chosen according to the number of HB donors/receptors (Figure 5). C6 is a hydrophobic dye with limited HB receptors. Its loading mainly depends on the hydrophobic interaction with the carrier PV_{31}-*b*-PD_{13}.[61] The DLS measurement revealed that the size of the C6-loaded NPs (C6@NPs) was about 153 nm with a narrow distribution (0.104, Table 2). The drug loading into NPs concentration was measured by UV−vis; then, the DLC and DLE, calculated by formulas, were 21.8% and 70.0%, respectively (Table 2). With the increase of HB donors/receptors, DLC and DLE of the cargo-loaded NPs increased accordingly. Then it was loaded into NPs according to the same method. The DOX@NPs reached up to 32.6% and 97.6% because of the abundant hydroxyl groups and amino groups of DOX that contribute significantly to the HB interaction between drug and polymer matrices. CDDP is a water-soluble drug, which usually possesses different kinds of HB donors or receptors (Figure 5). Especially, CDDP could

https://doi.org/10.1021/acs.biomac.1c01164
Biomacromolecules XXXX, XXX, XXX−XXX

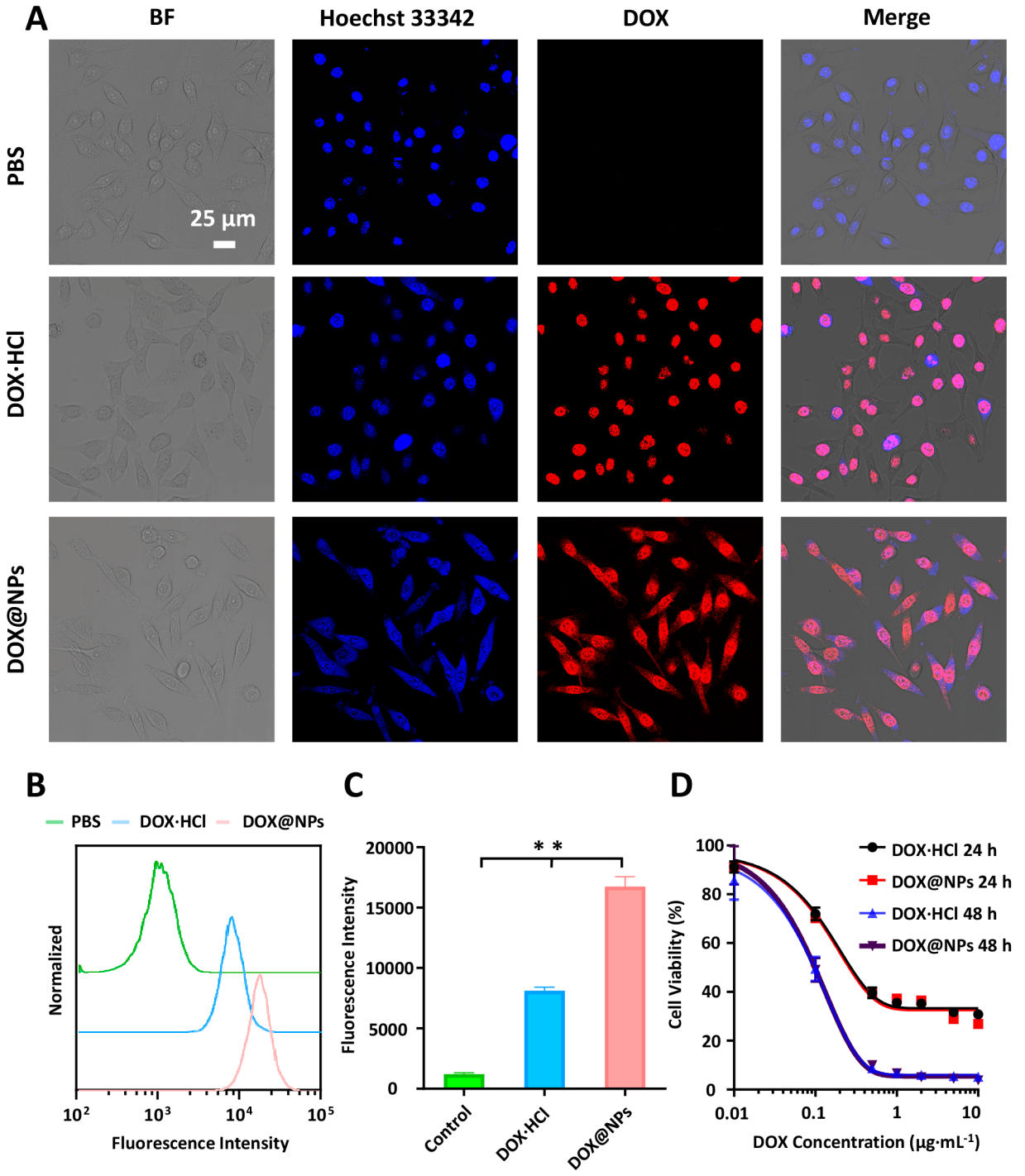

Figure 7. In vitro evaluation of intracellular uptake of DOX by fluorescence. (A) CLSM was utilized to visualize the cellular uptake behaviors of HepG2 cells treated with free DOX·HCl and DOX@NPs for 4 h. The DOX concentration was 2 μg mL^{-1}. The nuclear (blue) was stained with Hoechst 33342. Scale bar = 25 μm. (B) Flow cytometry and (C) statistics of cellular uptake of DOX after treating with free DOX·HCl and DOX@NPs for 4 h. Data were expressed as mean ± SD from three independent experiments. (D) The antitumor activity of free DOX·HCl and DOX@NPs against HepG2 cells for 24 and 48 h. The results were expressed as mean ± SD (n = 6); The p value was determined by two-way ANOVA analysis: $^{**}p < 0.01$.

also form a stable conjugation with carboxylate functional groups of PAA.[11] Therefore, its DLC and DLE in PV_{31}-*b*-PD_{13} NPs maintained at 31.2% and 78.2%, respectively. These results indicated that PAA-based DDS possessed an excellent drug loading capacity; different types of cargo molecules could be encapsulated via different interactions.

In Vitro Study on PAA-Based DDS. DOX was chosen as a representative drug to explore the properties of the PAA-based DDS (PV_{31}-*b*-PD_{13} NPs). As shown in the TEM images and DLS results (Figure 6A), the size of spherical DOX@NPs increased from around 101 to 255 nm before and after drug encapsulation, confirming that DOX was loaded into NPs successfully. The zeta potentials of blank NPs and DOX@NPs

https://doi.org/10.1021/acs.biomac.1c01164
Biomacromolecules XXXX, XXX, XXX−XXX

in water were found to be −40 and −37 mV, respectively (Figure S9). Figure 6B shows the DOX release profile of DOX@NPs in PBS buffers at pH 5.4, 6.0, and 7.4 (Figure 6B). About 45−55% DOX was released after a 12 h incubation, and the release ratio at pH 5.4 was slightly higher than that at pH 6.0 and 7.4. Meanwhile, blank NPs exhibited good cytocompatibility after being incubated with HepG2 cells and L929 cells for 24 and 48 h, respectively (Figures 6C and S10). Even though the concentration was up to 500 μg mL^{-1}, cell viability was higher than 85% after a 48 h incubation.

To explore the cellular internalized efficiency of DOX@NPs, HepG2 cells that coincubate with DOX@NPs or free DOX·HCl were observed at different time points (1, 5, 10, and 30 min) by CLSM. The red fluorescence of DOX enabled the visualization of the cells (Figure 6D). After a 1 min incubation, the DOX fluorescence was clearly visible in the cytoplasm of the cells in the DOX@NPs group; increasing incubation time resulted in significantly enhanced fluorescence intensity. Instead, there was rare fluorescence in the free DOX·HCl group, and the fluorescence was barely observed after 30 min incubation. Quantitative analysis by flow cytometry (Figure 6E and 6**F**) showed that the intracellular DOX from DOX@NPs was ∼3 times higher than that of the free DOX·HCl after 1 h incubation. This was the strong evidence demonstrated that the faster and higher internalization of DOX@NPs in contrast to the free DOX·HCl. These results were mainly due to the good biocompatibility of PAA-based DDS and their specific binding with cells.[62]

Intracellular drug distribution was determined by fluorescence colocalization. The nuclei of HepG2 cells were stained by Hoechst 33342 and exhibited a blue fluorescence. Considering the slow phagocytosis of free DOX·HCl, the incubation time was extended to 4 h. As Figure 7A shows, HepG2 cells were lit up in both groups. The fluorescence intensity of DOX@NPs was significantly higher than that of free DOX·HCl, which agreed with the aforementioned results (Figure 7B,C). Interestingly, intracellular DOX distribution in these two groups was different. Free DOX·HCl was mainly located in the nucleus, while DOX@NPs were distributed throughout the cells. This fact indicates free DOX·HCl and DOX@NPs were internalized with different pathways.[63] Free DOX·HCl entered into cells by free diffusion for its water-soluble property. Besides, free DOX·HCl penetrated into the cells unselectively and, thus, resulted in the entrance in nuclei.[64] Differently, the DOX@NPs were internalized into cells mainly via the endocytosis process and thus localized in endocytic compartments, such as endosomes and lysosomes. DOX, then, released from micelles and entered into nuclei.[65]

Additionally, the antitumor activity of the DOX@NPs against HepG2 cells was investigated (Figure 7D). As a well-known cytotoxic drug, free DOX·HCl was set as a positive control group. The half maximal inhibitory concentration (IC_{50}) of DOX@NPs and free DOX·HCl was 0.1547 and 0.1542 μg mL^{-1} after coincubation for 24 h, respectively, while DOX@NPs had a lower IC_{50} of 0.09 μg mL^{-1} toward HepG2 cells than that of free DOX·HCl (0.11 μg mL^{-1}) after 48 h incubation. Taken together, the result indicates a non-diminishing therapeutic effect of DOX@NPs.

4. CONCLUSIONS

In summary, the PET-RAFT technique was used to precisely synthesized PAA copolymers, including PV$_n$-*b*-PD$_m$, PF$_n$-*b*-PD$_m$, PV-OMe$_n$-*b*-PD$_m$, and PV-OMe$_n$-*b*-PS$_m$. By adjusting the molar ratio of hydrophilic/hydrophobic blocks and amino acid-based monomer types, the morphologies of the PAA copolymers could be modulated from spheres to rod-like, fiber, and lamellae. In-depth studies revealed that the HB interaction of carboxyl groups dominated the assembly behavior of PAA copolymers, while the interfacial attraction between hydrophobic blocks and the hydrophilic repulsion between hydrophilic blocks also made a significant contribution. PAA NPs could be used as great DDSs, encapsulating many types of cargos with high DLC (21∼32%) and a narrow distribution (0.1−0.2). Importantly, PAA-based DDSs exhibited a great potentiality in drug delivery because of its high drug loading capacity, good biocompatibility, fast endocytosis, and non-diminishing therapeutic effect. Based on these promising results, it is reasonable to foresee that these PAA-based NPs can be used as potential DDSs for disease treatment.

■ ASSOCIATED CONTENT

Supporting Information

The Supporting Information is available free of charge at https://pubs.acs.org/doi/10.1021/acs.biomac.1c01164.

Synthesis and characterization of monomers, polymers and assembled nanostructures, including the data of ^{1}H/^{13}C NMR, ESI-MS, EDS, GPC, DLS, and CCK8 (PDF)

■ AUTHOR INFORMATION

Corresponding Authors

Guofeng Li − *State Key Laboratory of Organic−Inorganic Composites, Beijing Advanced Innovation Center for Soft Matter Science and Engineering, Beijing Laboratory of Biomedical Materials, Beijing University of Chemical Technology, Beijing 100029, China*; Email: ligf@mail.buct.edu.cn

Jiangtao Xu − *Cluster for Advanced Macromolecular Design and Australian Centre for NanoMedicine, School of Chemical Engineering, UNSW Sydney, Sydney 2052, Australia*; orcid.org/0000-0002-9020-7018; Email: j.xu@unsw.edu.au

Xing Wang − *State Key Laboratory of Organic−Inorganic Composites, Beijing Advanced Innovation Center for Soft Matter Science and Engineering, Beijing Laboratory of Biomedical Materials, Beijing University of Chemical Technology, Beijing 100029, China*; orcid.org/0000-0002-9990-1479; Email: wangxing@mail.buct.edu.cn

Authors

Wenli Feng − *State Key Laboratory of Organic−Inorganic Composites, Beijing Advanced Innovation Center for Soft Matter Science and Engineering, Beijing Laboratory of Biomedical Materials, Beijing University of Chemical Technology, Beijing 100029, China*

Zixuan Huang − *Cluster for Advanced Macromolecular Design and Australian Centre for NanoMedicine, School of Chemical Engineering, UNSW Sydney, Sydney 2052, Australia*

Xiaoxu Kang − *State Key Laboratory of Organic−Inorganic Composites, Beijing Advanced Innovation Center for Soft Matter Science and Engineering, Beijing Laboratory of Biomedical Materials, Beijing University of Chemical Technology, Beijing 100029, China*

Dongdong Zhao − *State Key Laboratory of Organic−Inorganic Composites, Beijing Advanced Innovation*

https://doi.org/10.1021/acs.biomac.1c01164
Biomacromolecules XXXX, XXX, XXX−XXX

Center for Soft Matter Science and Engineering, Beijing Laboratory of Biomedical Materials, Beijing University of Chemical Technology, Beijing 100029, China

Haofei Li − *State Key Laboratory of Organic−Inorganic Composites, Beijing Advanced Innovation Center for Soft Matter Science and Engineering, Beijing Laboratory of Biomedical Materials, Beijing University of Chemical Technology, Beijing 100029, China*

Complete contact information is available at: https://pubs.acs.org/10.1021/acs.biomac.1c01164

Author Contributions

The manuscript was written through the contributions of all authors. All authors contributed to the final version of the manuscript.

Notes

The authors declare no competing financial interest.

■ ACKNOWLEDGMENTS

X.W. thanks the National Natural Science Foundation (21574008) and the Fundamental Research Funds for the Central Universities (BHYC1705B) of China for their financial support. J.X. acknowledges the Australian Research Council (ARC) for his Future Fellowship (FT160100095). G.L. thanks the National Natural Science Foundation (22005020) of China for the financial support.

■ REFERENCES

(1) Rahamim, V.; Azagury, A. Bioengineered Biomimetic and Bioinspired Noninvasive Drug Delivery Systems. *Adv. Funct. Mater.* **2021**, 2102033.

(2) Yamada, Y.; Sato, Y.; Nakamura, T.; Harashima, H. Evolution of Drug Delivery System from Viewpoint of Controlled Intracellular Trafficking and Selective Tissue Targeting Toward Future Nanomedicine. *J. Controlled Release* **2020**, *327*, 533−545.

(3) Zhang, C.; Liu, C.; He, W.; Jiao, D.; Liu, Z. Cross-linking-enhanced and Ultrasound-Mediated Drug Delivery: From Fabrication, Mechanisms to Translations. *Appl. Mater. Today* **2021**, *22*, 100897.

(4) Zou, Y.; Huang, B.; Cao, L.; Deng, Y.; Su, J. Tailored Mesoporous Inorganic Biomaterials: Assembly, Functionalization, and Drug Delivery Engineering. *Adv. Mater.* **2021**, *33*, 2005215.

(5) Qian, Q.; Zhu, L.; Zhu, X.; Sun, M.; Yan, D. Drug-Polymer Hybrid Macromolecular Engineering: Degradable PEG Integrated by Platinum(IV) for Cancer Therapy. *Matter* **2019**, *1*, 1618−1630.

(6) Huang, L.; Zhao, S.; Fang, F.; Xu, T.; Lan, M.; Zhang, J. Advances and Perspectives in Carrier-free Nanodrugs for Cancer Chemo-monotherapy and Combination Therapy. *Biomaterials* **2021**, *268*, 120557.

(7) Liu, Y.; Yang, G.; Baby, T.; Tengjisi; Chen, D.; Weitz, D. A.; Zhao, C. Stable Polymer Nanoparticles with Exceptionally High Drug Loading by Sequential Nanoprecipitation. *Angew. Chem.* **2020**, *132*, 4750−4758.

(8) Hassanzadeh, P.; Atyabi, F.; Dinarvand, R. The Significance of Artificial Intelligence in Drug Delivery System Design. *Adv. Drug Delivery Rev.* **2019**, *151*, 169−190.

(9) Mu, W.; Chu, Q.; Liu, Y.; Zhang, N. A Review on Nano-Based Drug Delivery System for Cancer Chemoimmunotherapy. *Nano-Micro Lett.* **2020**, *12*, 1−24.

(10) Zhong, H.; Chan, G.; Hu, Y.; Hu, H.; Ouyang, D. A Comprehensive Map of FDA-Approved Pharmaceutical Products. *Pharmaceutics* **2018**, *10*, 263.

(11) Cheng, C.; Meng, Y.; Zhang, Z.; Li, Y.; Zhang, Q. Tumoral Acidic pH-Responsive cis-Diaminodichloroplatinum-Incorporated Cy5.5-PEG-g-A-HA Nanoparticles for Targeting Delivery of CDDP against Cervical Cancer. *ACS Appl. Mater. Interfaces* **2018**, *10*, 26882−26892.

(12) Scarano, W.; De Souza, P.; Stenzel, M. H. Dual-drug Delivery of Curcumin and Platinum Drugs in Polymeric Micelles Enhances the Synergistic Effects: A Double Act for the Treatment of Multidrug-resistant Cancer. *Biomater. Sci.* **2015**, *3*, 163−174.

(13) Shi, X.; Bai, S.; Yang, C.; Ma, X.; Hou, M.; Chen, J.; Xue, P.; Li, C. M.; Kang, Y.; Xu, Z. Improving the Carrier Stability and Drug Loading of Unimolecular Micelle-based Nanotherapeutics for Acid-activated Drug Delivery and Enhanced Antitumor Therapy. *J. Mater. Chem. B* **2018**, *6*, 5549−5561.

(14) Li, X.; Xie, C.; Xia, H.; Wang, Z. pH and Ultrasound Dual-Responsive Polydopamine-Coated Mesoporous Silica Nanoparticles for Controlled Drug Delivery. *Langmuir* **2018**, *34*, 9974−9981.

(15) Vong, L. B.; Trinh, N.; Nagasaki, Y. Design of Amino Acid-based Self-assembled Nano-drugs for Therapeutic Applications. *J. Controlled Release* **2020**, *326*, 140−149.

(16) Zheng, C.; Zhang, X. G.; Sun, L.; Zhang, Z. P.; Li, C. X. Biodegradable and Redox-Responsive Chitosan/poly(l-aspartic acid) Submicron Capsules for Transmucosal Delivery of Proteins and Peptides. *J. Mater. Sci.: Mater. Med.* **2013**, *24*, 931−939.

(17) Sanda, F.; Endo, T. Syntheses and Functions of Polymers Based on Amino Acids. *Macromol. Chem. Phys.* **1999**, *200*, 2651−2661.

(18) Mori, H.; Matsuyama, M.; Endo, T. Double-Hydrophilic and Amphiphilic Block Copolymers Synthesized by RAFT Polymerization of Monomers Carrying Chiral Amino Acids. *Macromol. Chem. Phys.* **2009**, *210*, 217−229.

(19) Mori, H.; Matsuyama, M.; Sutoh, K.; Endo, T. RAFT Polymerization of Acrylamide Derivatives Containing L-Phenylalanine Moiety. *Macromolecules* **2006**, *39*, 4351−4360.

(20) Liu, Y.; Yin, L. α-Amino Acid N-carboxyanhydride (NCA)-derived Synthetic Polypeptides for Nucleic Acids Delivery. *Adv. Drug Delivery Rev.* **2021**, *171*, 139−163.

(21) Zhou, X.; Li, Z. Advances and Biomedical Applications of Polypeptide Hydrogels Derived from α-Amino Acid N-Carboxyanhydride (NCA) Polymerizations. *Adv. Healthcare Mater.* **2018**, *7*, 1800020.

(22) Jiang, J.; Zhang, X.; Fan, Z.; Du, J. Ring-Opening Polymerization of N-Carboxyanhydride-Induced Self-Assembly for Fabricating Biodegradable Polymer Vesicles. *ACS Macro Lett.* **2019**, *8*, 1216−1221.

(23) Jacobs, J.; Pavlović, D.; Prydderch, H.; Moradi, M.; Ibarboure, E.; Heuts, J. P. A.; Lecommandoux, S.; Heise, A. Polypeptide Nanoparticles Obtained from Emulsion Polymerization of Amino Acid N-Carboxyanhydrides. *J. Am. Chem. Soc.* **2019**, *141*, 12522−12526.

(24) Nandi, M.; Maiti, B.; Banerjee, S.; De, P. Hydrogen Bonding Driven Self-assembly of Side-chain Amino Acid and Fatty Acid Appended Poly(methacrylate)s: Gelation and Application in Oil Spill Recovery. *J. Polym. Sci., Part A: Polym. Chem.* **2019**, *57*, 511−521.

(25) Deming, T. J. Synthesis of Side-Chain Modified Polypeptides. *Chem. Rev.* **2016**, *116*, 786−808.

(26) Qi, G. B.; Gao, Y. J.; Wang, L.; Wang, H. Self-Assembled Peptide-Based Nanomaterials for Biomedical Imaging and Therapy. *Adv. Mater.* **2018**, *30*, 1703444.

(27) Takeda, K. M.; Yamasaki, Y.; Dirisala, A.; Ikeda, S.; Tockary, T. A.; Toh, K.; Osada, K.; Kataoka, K. Effect of Shear Stress on Structure and fFunction of Polyplex Micelles From Poly(ethylene glycol)-poly(l-lysine) Block Copolymers as Systemic Gene Delivery Carrier. *Biomaterials* **2017**, *126*, 31−38.

(28) Yoo, J.; Lee, D.; Gujrati, V.; Rejinold, N. S.; Lekshmi, K. M.; Uthaman, S.; Jeong, C.; Park, I.; Jon, S.; Kim, Y. Bioreducible Branched Poly(modified nona-arginine) Cell-penetrating Peptide as A Novel Gene Delivery Platform. *J. Controlled Release* **2017**, *246*, 142−154.

(29) Zhou, M.; Hou, T.; Li, J.; Yu, S.; Xu, Z.; Yin, M.; Wang, J.; Wang, X. Self-Propelled and Targeted Drug Delivery of Poly(aspartic acid)/Iron-Zinc Microrocket in the Stomach. *ACS Nano* **2019**, *13*, 1324−1332.

(30) Teng, W.; Jia, F.; Han, H.; Qin, Z.; Jin, Q.; Ji, J. Polyamino Acid-based Gemcitabine Nanocarriers for Targeted Intracellular Drug Delivery. *Polym. Chem.* **2017**, *8*, 2490−2498.
(31) Liu, S.; Ono, R. J.; Wu, H.; Teo, J. Y.; Liang, Z. C.; Xu, K.; Zhang, M.; Zhong, G.; Tan, J. P. K.; Ng, M.; Yang, C.; Chan, J.; Ji, Z.; Bao, C.; Kumar, K.; Gao, S.; Lee, A.; Fevre, M.; Dong, H.; Ying, J. Y.; Li, L.; Fan, W.; Hedrick, J. L.; Yang, Y. Y. Highly Potent Antimicrobial Polyionenes with Rapid Killing Kinetics, Skin Biocompatibility and In Vivo Bactericidal Activity. *Biomaterials* **2017**, *127*, 36−48.
(32) Holowka, E. P.; Pochan, D. J.; Deming, T. J. Charged Polypeptide Vesicles with Controllable Diameter. *J. Am. Chem. Soc.* **2005**, *127*, 12423−12428.
(33) Jena, S. S.; Roy, S. G.; Azmeera, V.; De, P. Solvent-dependent Self-assembly Behaviour of Block Copolymers Having Side-chain Amino Acid and Fatty Acid Block Segments. *React. Funct. Polym.* **2016**, *99*, 26−34.
(34) Bauri, K.; Maiti, B.; De, P. Leucine-Based Block Copolymer Nano-Objects via Polymerization-Induced Self-Assembly (PISA). *Macromol. Symp.* **2016**, *369*, 101−107.
(35) Bauri, K.; Narayanan, A.; Haldar, U.; De, P. Polymerization-induced Self-assembly Driving Chiral Nanostructured Materials. *Polym. Chem.* **2015**, *6*, 6152−6162.
(36) Machado, C. A.; Smith, I. R.; Savin, D. A. Self-Assembly of Oligo- and Polypeptide-Based Amphiphiles: Recent Advances and Future Possibilities. *Macromolecules* **2019**, *52*, 1899−1911.
(37) Xu, H.; Yao, Q.; Cai, C.; Gou, J.; Zhang, Y.; Zhong, H.; Tang, X. Amphiphilic Poly(amino acid) Based Micelles Applied to Drug Delivery: The In Vitro and In Vivo Challenges and the Corresponding Potential Strategies. *J. Controlled Release* **2015**, *199*, 84−97.
(38) Zhao, J.; Qu, Y.; Chen, H.; Xu, R.; Yu, Q.; Yang, P. Self-assembled Proteinaceous Wound Dressings Attenuate Secondary Trauma and Improve Wound Healing In Vivo. *J. Mater. Chem. B* **2018**, *6*, 4645−4655.
(39) Li, G.; Feng, W.; Corrigan, N.; Boyer, C.; Wang, X.; Xu, J. Precise Synthesis of Poly(N-acryloyl amino acid) Through Photo-induced Living Polymerization. *Polym. Chem.* **2018**, *9*, 2733−2745.
(40) Wang, X.; Gan, H.; Zhang, M.; Sun, T. Modulating Cell Behaviors on Chiral Polymer Brush Films with Different Hydrophobic Side Groups. *Langmuir* **2012**, *28*, 2791−2798.
(41) Feng, W.; Li, G.; Tao, L.; Wei, Y.; Wang, X. Poly(amino acid)s-based Star AIEgens for Cell Uptake with pH-response and Chiral Difference. *Colloids Surf., B* **2021**, *202*, 111687.
(42) Lv, S.; Wu, Y.; Cai, K.; He, H.; Li, Y.; Lan, M.; Chen, X.; Cheng, J.; Yin, L. High Drug Loading and Sub-Quantitative Loading Efficiency of Polymeric Micelles Driven by Donor−Receptor Coordination Interactions. *J. Am. Chem. Soc.* **2018**, *140*, 1235−1238.
(43) Mohar, M.; Das, T.; Ghosh, N. N. Development of a Tripeptide based Arginine Sensor via Applying the Concept of Molecular Engineering. *Colloid Interface Sci. Commun.* **2021**, *41*, 100364.
(44) Choucair, A.; Lavigueur, C.; Eisenberg, A. Polystyrene-b-poly(acrylic acid) Vesicle Size Control Using Solution Properties and Hydrophilic Block Length. *Langmuir* **2004**, *20*, 3894−3900.
(45) Zhu, Y.; Liu, L.; Du, J. Probing into Homopolymer Self-Assembly: How Does Hydrogen Bonding Influence Morphology? *Macromolecules* **2013**, *46*, 194−203.
(46) Fung, S. Y.; Yang, H.; Sadatmousavi, P.; Sheng, Y.; Mamo, T.; Nazarian, R.; Chen, P. Amino Acid Pairing for De Novo Design of Self-Assembling Peptides and Their Drug Delivery Potential. *Adv. Funct. Mater.* **2011**, *21*, 2456−2464.
(47) Tashiro, S.; Nakata, K.; Hayashi, R.; Shionoya, M. Multipoint Hydrogen Bonding-Based Molecular Recognition of Amino Acids and Peptide Derivatives in a Porous Metal-Macrocycle Framework: Residue-Specificity, Diastereoselectivity, and Conformational Control. *Small* **2021**, *17*, 2005803.
(48) Mai, Y.; Eisenberg, A. Self-assembly of Block Copolymers. *Chem. Soc. Rev.* **2012**, *41*, 5969−5985.
(49) Yao, Y.; Zhou, D.; Shen, Y.; Wu, H.; Wang, H. Morphology-controllable Amphiphilic Cellulose Microgels Made from Self-assembly of Hydrophobic Long-chain Bromide-alkylated-cellulose/gelatin Copolymer. *Carbohydr. Polym.* **2021**, *269*, 118265.
(50) Han, L.; Wang, M.; Jia, X.; Chen, W.; Qian, H.; He, F. Uniform Two-dimensional Square Assemblies from Conjugated Block Copolymers Driven by $\pi-\pi$ Interactions with Controllable Sizes. *Nat. Commun.* **2018**, *9*, 1−12.
(51) Sun, H.; Liu, D.; Du, J. Nanobowls with Controlled Openings and Interior Holes Driven by the Synergy of Hydrogen Bonding and $\pi-\pi$ Interaction. *Chem. Sci.* **2019**, *10*, 657−664.
(52) Wong, C. K.; Mason, A. F.; Stenzel, M. H.; Thordarson, P. Formation of Non-spherical Polymersomes Driven by Hydrophobic Directional Aromatic Perylene Interactions. *Nat. Commun.* **2017**, *8*, 1−10.
(53) Burke, S. E.; Eisenberg, A. Kinetics and Mechanisms of the Sphere-to-Rod and Rod-to-Sphere Transitions in the Ternary System PS310-b-PAA52/Dioxane/Water. *Langmuir* **2001**, *17*, 6705−6714.
(54) Ding, X.; Han, N.; Wang, J.; Sun, Y.; Ruan, G. Effects of Organic Solvents on the Structures of Micellar Nanocrystals. *RSC Adv.* **2017**, *7*, 16131−16138.
(55) Nonappa; Haataja, J. S.; Timonen, J. V. I.; Malola, S.; Engelhardt, P.; Houbenov, N.; Lahtinen, M.; Häkkinen, H.; Ikkala, O. Reversible Supracolloidal Self-Assembly of Cobalt Nanoparticles to Hollow Capsids and Their Superstructures. *Angew. Chem.* **2017**, *129*, 6573−6577.
(56) Adler-Abramovich, L.; Vaks, L.; Carny, O.; Trudler, D.; Magno, A.; Caflisch, A.; Frenkel, D.; Gazit, E. Phenylalanine Assembly into Toxic Fibrils Suggests Amyloid Etiology in Phenylketonuria. *Nat. Chem. Biol.* **2012**, *8*, 701−706.
(57) Ye, Q.; Huo, M.; Zeng, M.; Liu, L.; Peng, L.; Wang, X.; Yuan, J. Photoinduced Reversible Worm-to-Vesicle Transformation of Azo-Containing Block Copolymer Assemblies Prepared by Polymerization-Induced Self-Assembly. *Macromolecules* **2018**, *51*, 3308−3314.
(58) Oh, T.; Nagao, M.; Hoshino, Y.; Miura, Y. Self-Assembly of a Double Hydrophilic Block Glycopolymer and the Investigation of Its Mechanism. *Langmuir* **2018**, *34*, 8591−8598.
(59) Li, C.; Chen, C.; Li, S.; Rasheed, T.; Huang, P.; Huang, T.; Zhang, Y.; Huang, W.; Zhou, Y. Self-assembly and Functionalization of Alternating Copolymer Vesicles. *Polym. Chem.* **2017**, *8*, 4688−4695.
(60) Sun, Z.; Yi, Z.; Zhang, H.; Ma, X.; Su, W.; Sun, X.; Li, X. Bio-responsive Alginate-Keratin Composite Nanogels with Enhanced Drug Loading Efficiency for Cancer Therapy. *Carbohydr. Polym.* **2017**, *175*, 159−169.
(61) Luo, Y.; Teng, Z.; Li, Y.; Wang, Q. Solid Lipid Nanoparticles for Oral Drug Delivery: Chitosan Coating Improves Stability, Controlled Delivery, Mucoadhesion and Cellular Uptake. *Carbohydr. Polym.* **2015**, *122*, 221−229.
(62) Zhu, Z.; Tian, D.; Gao, P.; Wang, K.; Li, Y.; Shu, X.; Zhu, J.; Zhao, Q. Cell-Penetrating Peptides Transport Noncovalently Linked Thermally Activated Delayed Fluorescence Nanoparticles for Time-Resolved Luminescence Imaging. *J. Am. Chem. Soc.* **2018**, *140*, 17484−17491.
(63) Chen, Z.; Yang, S.; Liu, X.; Gao, Y.; Dong, X.; Lai, X.; Zhu, M.; Feng, H.; Zhu, X.; Lu, Q.; Zhao, M.; Chen, H.; Lovell, J. F.; Fang, C. Nanobowl-Supported Liposomes Improve Drug Loading and Delivery. *Nano Lett.* **2020**, *20*, 4177−4187.
(64) Liang, K.; Chung, J. E.; Gao, S. J.; Yongvongsoontorn, N.; Kurisawa, M. Highly Augmented Drug Loading and Stability of Micellar Nanocomplexes Composed of Doxorubicin and Poly(ethylene glycol)-Green Tea Catechin Conjugate for Cancer Therapy. *Adv. Mater.* **2018**, *30*, 1706963.
(65) Yan, J.; Zhang, N.; Zhang, Z.; Zhu, W.; Li, B.; Li, L.; Pu, Y.; He, B. Redox-responsive Polyethyleneimine/tetrahedron DNA/doxorubicin Nanocomplexes for Deep Cell/tissue Penetration to Overcome Multidrug Resistance. *J. Controlled Release* **2021**, *329*, 36−49.

https://doi.org/10.1021/acs.biomac.1c01164
Biomacromolecules XXXX, XXX, XXX−XXX